

Impact of Meteorological Factors on the Mesoscale Morphology of Cloud Streets during a Cold-Air Outbreak over the Western North Atlantic

JINGYI CHEN,^a HAILONG WANG,^a XIANGYU LI,^a DAVID PAINEMAL,^{b,c} ARMIN SOROOSHIAN,^{d,e}
KENNETH LEE THORNHILL,^{c,b} CLAIRE ROBINSON,^{c,b} AND TAYLOR SHINGLER^c

^a Pacific Northwest National Laboratory, Richland, Washington

^b Science Systems and Applications, Inc., Hampton, Virginia

^c NASA Langley Research Center, Hampton, Virginia

^d Department of Chemical and Environmental Engineering, The University of Arizona, Tucson, Arizona

^e Department of Hydrology and Atmospheric Sciences, The University of Arizona, Tucson, Arizona

(Manuscript received 11 February 2022, in final form 1 June 2022)

ABSTRACT: Postfrontal clouds (PFC) are ubiquitous in the marine boundary layer, and their morphology is essential to estimating the radiation budget in weather and climate models. Here we examine the roles of sea surface temperature (SST) and meteorological factors in controlling the mesoscale morphology and evolution of shallow clouds associated with a cold-air outbreak that occurred on 1 March 2020 during phase I of the Aerosol Cloud Meteorology Interactions over the Western Atlantic Experiment (ACTIVATE). Our results show that the simulated PFC structure and ambient conditions by the Weather Research and Forecasting (WRF) Model are generally consistent with observations from *GOES-16* and dropsonde measurements. We also examine the thermodynamical and dynamical influences in the cloud mesoscale morphology using WRF sensitivity experiments driven by two meteorological forcing datasets with different domain-mean SST and spatial gradients, which lead to dissimilar values of hydrometeor water path and cloud core fraction. The SST from ERA5 leads to weaker stability and higher inversion height than the SST from FNL does. In addition, the use of large-scale meteorological forcings from ERA5 yields a distinctive time evolution of wind direction shear in the inner domain, which favors the formation and persistence of longer cloud rolls. Both factors contribute to a change in the time evolution of domain-mean water path and cloud core fraction of cloud streets. Our study takes advantage of the simulation driven by the differences between two large-scale forcing datasets to illustrate the importance of SST and wind direction shear in the cloud street morphology in a realistic scenario.

KEYWORDS: Cloud cover; Clouds; Cloud resolving models

1. Introduction

Clouds in the wake of cold fronts, namely, postfrontal clouds (PFCs), are populated at low levels in the marine boundary layer (Naud et al. 2018; Agee 1987). These clouds influence the reflectivity and vertical turbulent transport in the boundary layer (Gryschka et al. 2014). Predicting cloud cover and structure of such ubiquitous low-level clouds is essential to estimating precipitation and radiation in weather and climate models. However, their prediction relies on multiple processes smaller than typical numerical model grids. Thus, general circulation models (GCMs) and also reanalyses datasets have difficulty representing both the correct amount and the coherent structure of the distribution of such clouds (Naud et al. 2014; Williams et al. 2013).

In postfrontal regions, satellite imagery often exhibits a cloud street pattern in a form of extended parallel cumulus clouds over coastal waters (Walter and Overland 1984; Atkinson and Zhang 1996). Those cloud street cases are frequently observed to the east of land and over relatively warm sea surfaces during the cold-air outbreak events, for example, in the northwest Pacific Ocean (e.g., Wu and Chen 2021; Chen et al. 2019), over the western Gulf Stream (e.g., Chou and Ferguson 1991),

or the Greenland Sea (e.g., Chlond 1992). Those cloud streets are usually oriented almost along the mean wind direction, with a roll wavelength ranging between 2 and 20 km. The downward longitudinal extension of these rolls into helical eddies (Etling and Brown 1993) can reach between 10 and 100 km. The most common explanation of cloud streets is that they are the result of convection (i.e., thermal instability) occurring with strong wind shear (i.e., dynamic instability). Mason (1983) examined the influence of the Monin–Obukhov length (Foken 2006) on roll vortices by two-dimensional (2D) simulations and concluded that typical large-scale roll vortices are essentially buoyancy driven with nondominant shear production. Zurn–Birkhimer et al. (2005) showed that the coherent structures grow in a building block fashion with buoyancy as the dominating physical mechanism for organizing the convection (even in the presence of substantial wind shear).

Besides the interest in the formation of cloud streets, the morphology of cloud streets is also of great interest. Gryschka and Raasch (2005) found an angle of 30° between the coherent-structure axis and the geostrophic wind direction. Salesky et al. (2017) found that the transition from roll to the cellular cloud organization occurs gradually over a range of stability conditions, from neutral to the highly unstable and convective boundary layer. In addition, Wu and Chen (2021) examined the response of cloud streets to aerosols, which revealed a clear aerosol albedo effect but a lack of the indirect effect on liquid cloud water

Corresponding authors: Jingyi Chen, jingyi.chen@pnnl.gov; Hailong Wang, hailong.wang@pnnl.gov

DOI: 10.1175/JAS-D-22-0034.1

© 2022 American Meteorological Society. For information regarding reuse of this content and general copyright information, consult the AMS Copyright Policy (www.ametsoc.org/PUBSReuseLicenses).

due to the interplay between dynamical and thermodynamical mechanisms.

Inaccurate and inconsistent parameterization schemes have been thought to be one critical source of the bias in simulating the amount of PFCs in GCMs (Lamraoui et al. 2019; Field et al. 2014). Lamraoui et al. (2019) found that many factors significantly impact the distribution of such clouds by their distinct configurations with different planetary boundary layer (PBL) and convection schemes. Those factors include the strength of PBL decoupling, vertical wind shear, entrainment and detrainment rates in shallow convection, and the occurrence of drizzle. Convective schemes modulate the warming and moistening of the environment through clouds by parameterizing the vertical transport of mass flux. PBL schemes regulate the thermodynamic structure of the subcloud layer through the interaction with the large-scale flow and surface fluxes. Lamraoui et al. (2019) also found that microphysics schemes have weaker impacts on the cloud amount than the PBL and convective schemes. Simulations at a mesh size smaller than the typical climate model grid box are often used to reproduce many features of PFCs and improve the understanding of the mechanisms behind their formation and evolution (Abel et al. 2017; Kawase et al. 2005; Kazemirad and Miller 2020; Mechem et al. 2010; Wu and Chen 2021). Such fine-mesh-sized simulations (i.e., spatial grid spacing at ~ 1 km) has proved to be able to capture the secondary mesoscale circulations, which are necessary to form the spatial patterns of observed PFCs including cloud street (e.g., Etling and Brown 1993) and mesoscale cellular clouds (e.g., Wang and Feingold 2009). Liu et al. (2004) for the first time performed three-dimensional (3D) simulations at a grid spacing of 500 m to explicitly resolve convection in a domain sufficiently large to allow for the evolution of multiple cloud rolls in the PFC region. Lai et al. (2020) showed increasing resolution from 27 to ~ 0.1 km leads to a transition from stratiform-like clouds to roll-like structures along with the transition from a more buoyancy-driven PBL to a more shear driven PBL.

PFCs usually exist on the downstream side of the geostrophic wind, so the uncertainties with the upstream information also bias the simulation of cloud amount and structure. Much effort has been invested into constructing the large-scale forcings for the limited area simulations (e.g., Endo et al. 2015; Li et al. 2021). Particularly for PFCs, surface fluxes, wind and moisture are assumed to be deterministic factors for the formation of cloud streets including their morphology (LeMone 1973; Spensberger and Spengler 2021; Babić and De Wekker 2019). Here we present a case study associated with a cold-air outbreak during the Aerosol Cloud Meteorology Interactions over the Western Atlantic Experiment (ACTIVATE) field campaign. We performed sensitivity studies for various large-scale forcing datasets (as initial and boundary conditions for the regional model) to reveal the impact of forcing on the mesoscale morphology of cloud streets in the post-frontal region. The remaining content of this study is organized as follows. Section 2 introduces the case study and model configurations. Section 3 shows the comparisons of cloud structure and PBL profiles between simulations and

observations, and the sensitivities to the forcings. Section 4 summarizes the conclusions and discussion.

2. Case study and model setup

ACTIVATE is designed to understand the variability of marine boundary layer clouds and the multiple feedbacks that hinder scientists' efforts to attribute changes in cloud properties to aerosol perturbations over the western North Atlantic Ocean (WNAO) including cold-air outbreak events (CAOs) (Sorooshian et al. 2019; Dadashazar et al. 2021). The WNAO region is subject to a distinct range of lower tropospheric stability (LTS) values that give rise to wide liquid water path variability. PFCs prevail in this region during the winter season and they represent a cloud type suffering large underrepresentation in climate models with only a few-percent coverage compared to remote sensing observations of 15%–20% (Sorooshian et al. 2020; Field et al. 2017, 2014; Painemal et al. 2021a). To acquire collocated measurements within the PBL, simultaneous sampling by in situ and remote sensing instruments are available from two aircraft along with dropsondes and satellite measurements. This aims at improving the understanding in the meteorological controls on marine boundary layer clouds, including LTS, sea surface temperature (SST), winds, horizontal advection, and large-scale subsidence. ACTIVATE includes 3 years of flights (2020–22) in different seasons, and this work focuses on data from the first year. Li et al. (2021) derived large-scale divergence and surface turbulent fluxes from the ACTIVATE measurements and reanalysis products for two CAOs and evaluated the simulated PBL state and clouds by large-eddy simulation (LES; with a grid spacing of 100–300 m) with measurements. Their work paves the path for investigating aerosol–cloud–meteorology interactions using LES informed and evaluated by ACTIVATE field measurements.

Cloud products estimated from the *GOES-16* Advanced Baseline Imager (ABI) are derived using the NASA's Clouds and the Earth's Radiant Energy System (CERES) Edition 4 algorithms (Minnis et al. 2011, 2021) adapted to ingest ABI radiometric channels, and integrated into the NASA Satellite Cloud and Radiation Property retrieval System (SatCORPS; e.g., Minnis et al. 2008; Painemal et al. 2021b). For ACTIVATE, *GOES-16* retrievals were produced at 2 km pixel resolution every 20 min.

This study focuses on one of the two CAO events reported in Li et al. (2021), which took place on 1 March 2020 with PFCs appearing in the WNAO region. Our goal is to examine the mesoscale morphology of PFCs in a large domain with realistic large-scale forcings and boundary conditions. Figure 1 shows cloud optical depth over four consecutive days from 27 February to 1 March. A cold front passed the WNAO region on 27 February with the frontal clouds persisting in the southeast of WNAO domain at least ~ 3 days afterward. On 29 February, a cloud deck was observed over WNAO that moved eastward on 1 March. Our focused case on 1 March includes those broken PFCs behind trough. Figure 2 shows the liquid water path (LWP) and ice water path (IWP) from *GOES-16* 2 km spatial resolution at 0801 and 1001 eastern

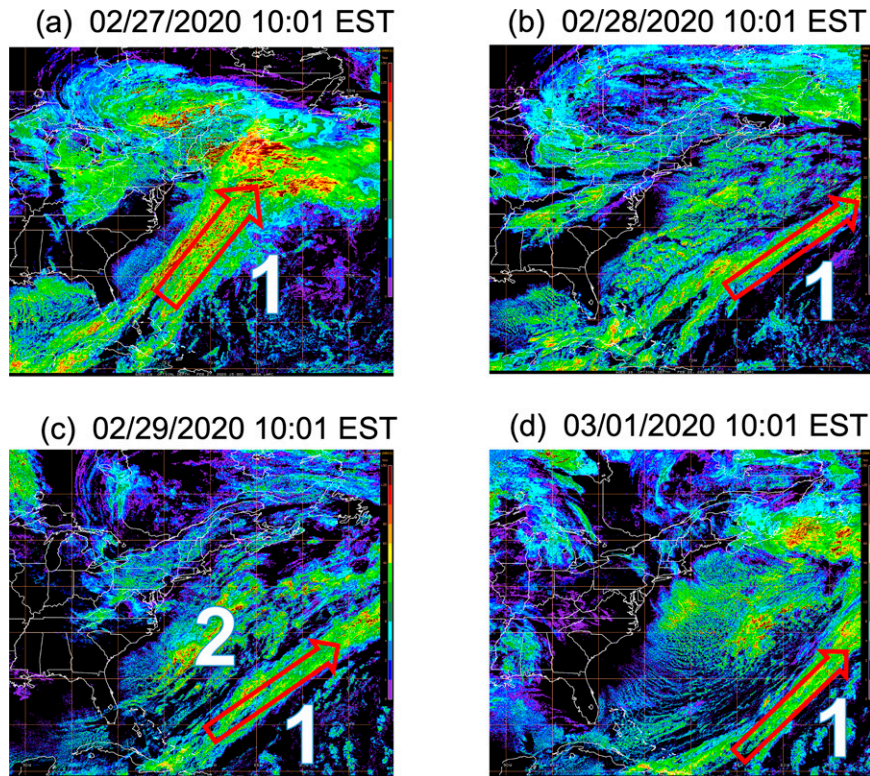


FIG. 1. Cloud optical depth on (a) 27 Feb, (b) 28 Feb, (c) 29 Feb, and (d) 1 Mar at 1501 UTC (1001 EST) each day retrieved from *GOES-16*. The red arrows indicate the alignments of the first cold-frontal clouds passing over the WNAO region on 27 Feb. The number indicates the first cold-frontal events and the cloud deck in postfrontal region.

standard time (EST). In the top row of Fig. 2, the large cloudy area in southwest shows the trough and a large area of PFCs to the west. That PFC was dissipating in the local morning forming line and cellular structure, as the zoom-in figure in the bottom row shows. Vertical profiles of air pressure P , temperature T , relative humidity RH, and horizontal velocities u and v were measured by eleven dropsondes released from NASA Langley Research Center's King Air aircraft. The dropsonde measurements (i.e., red dots) were released between 0951 and 1045 UTC measuring meteorological parameters within the PBL and lower free troposphere. We use both *GOES-16* and dropsondes to evaluate the model simulations in section 3.

We use the Weather Research and Forecasting (WRF) Model V4.2 to simulate the mesoscale features of PFCs (Skamarock et al. 2019). The nested-domain simulations are designed to have an outer domain covering a larger area but with coarser resolution and an inner domain covering a smaller area but with higher resolution. The outer domain of the simulations includes most of the WNAO region, covering the eastern coast of the United States and the northwest Atlantic Ocean (Sorooshian et al. 2020). In this case study, the outer domain covers the location of the cold front and the whole postfrontal region. The lateral side of the outer domain size is 1650 km using a 3 km horizontal grid spacing. It has

150 vertical levels extending up to 16 km with a constant ~ 46 m grid spacing near the surface up to 6 km. The inner domain adopts the same vertical grid spacing. Each side of the square inner domain is 450 km with a 1 km horizontal grid spacing, covering the dropsonde sampling area and the cloud streets. We use two-way nesting (Harris and Durran 2010), so that the inner domain higher-resolution features can propagate to the outer domain and feedback to the inner domain in later time steps, while in the one-way nesting inner domain does not impact outer domain. We use the Morrison two-moment microphysics scheme (Morrison et al. 2005), Yonsei University PBL scheme (YSU; Hong and Lim 2006), and Rapid Radiative Transfer Model for GCMs (RRTMG) scheme for longwave and shortwave radiation (Iacono et al. 2008) to represent the subgrid-scale processes. An interactive land option is turned on with the unified Noah land surface model (Chen and Dudhia 2001). We turned off the subgrid convection parameterization because it is well known that subgrid-convection-off simulations show better consistency than subgrid-convection-on simulations at gray-zone scale (Field et al. 2017).

All simulations mentioned in section 3 are summarized in Table 1. The sensitivity simulations shown in Table 1 are constructed by swapping initial and boundary condition variables between the fifth generation of atmospheric reanalysis from European Centre for Medium-Range Weather Forecasts

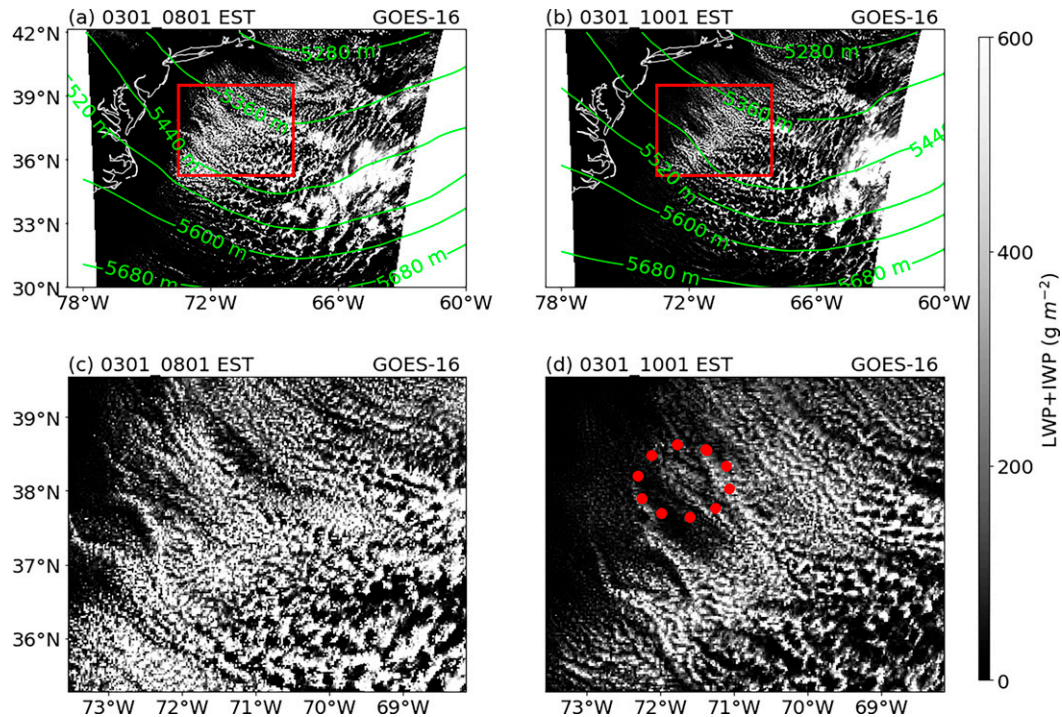


FIG. 2. Liquid water path (LWP) or ice water path (IWP) from *GOES-16* (2 km) for (a),(b) a larger area of the WNAO and (c),(d) a zoom-in region with cloud street and open cellular clouds at (a),(c) 0801 and (b),(d) 1001 EST. Red rectangles indicate where the zoom-in region is. Green contours are the geopotential heights at 500 hPa from ERA5. Red dots show dropsonde locations.

(ERA5) and National Centers for Environmental Prediction (NCEP) Final Operational Global Analysis data (FNL). ERA5 is the latest generation of global reanalysis dataset produced by the European Centre for Medium-Range Weather Forecasts (ECMWF), which provides dozens of commonly used land surface and atmospheric variables with temporal coverage from 1950 to present (Hersbach et al. 2020). By assimilating a large number of ground-based observations, atmospheric sounding data, and remote sensing data, ERA5 provides reasonable spatial and temporal variability of precipitation at a large scale. Particularly in regions with dense ground-based data such as in North America and Europe, ERA5 shows better performance after assimilating those

ground-based observations (Tarek et al. 2020; Bandhauer et al. 2021). NCEP-FNL data (National Centers for Environmental Prediction 2000) are also widely used to generate forcing for limited-area models (e.g., Fast et al. 2019). NCEP-FNL provides the final operational global analysis data from the Global Forecasting System of the National Centers for Environment Prediction. Note that here we do not aim to evaluate different datasets but rather conduct sensitivity simulations with different yet consistent and realistic surface and boundary conditions. The goal is to show how differences in surface heating, wind shear, and moisture between ERA5 and FNL impact the evolution and characteristics of cloud streets in the WNAO PFC region on 1 March 2020. We construct the sensitivity studies

TABLE 1. This table summarizes the simulations mentioned in section 3c(1). Differences apply to the initial and boundary conditions. SST refers to sea surface temperature, and METEO refers to the geopotential height, potential temperature, winds, and water vapor mixing ratio.

Simulation name	Configurations
ERA5	Control simulation, driven by ERA5 reanalysis datasets
ERA5(FNL_SST)	As in ERA5, except that the SST is from FNL
ERA5(FNL_METEO)	As in ERA5, except that geopotential height, potential temperature, winds, and water vapor mixing ratio are from FNL
FNL	As in ERA5, except that it is driven by FNL analysis datasets
FNL(ERA5_SST)	As in FNL, except that SST is from ERA5
FNL(ERA5_METEO)	As in FNL, except that geopotential height, potential temperature, winds, and water vapor mixing ratio are from ERA5

TABLE 2. Summary of terms and variables used to characterize features and morphology of cloud streets.

Term	Definition
Total water path (WP)	Vertically integrated hydrometeor mixing ratio including cloud, rain, ice, graupel, and snow
Cloud core fraction	WP/WP _{sm} , where the subscript “sm” denotes “smoothed” cloud field
Cloud mask	Area where cloud core fraction WP/WP _{sm} > 0.8
Aspect ratio of cloud mask (L_l/L_s)	Ratio of the longest dimension (L_l) to the shortest dimension (L_s) of the defined cloud mask
Angle between cloud alignment and wind direction	Angle between the longest dimension of cloud mask and wind direction
Instability	$\Theta_{\text{surf}} - \Theta_{850\text{hPa}}$
Wind direction shear	$WD_{850\text{hPa}} - WD_{950\text{hPa}}$ averaged below clouds with $L_l/L_s > 2$
Long roll	$L_l/L_s > 6$

by swapping variables between ERA5 and FNL and analyze the response of simulated cloud street morphology to the differences between those two forcing datasets. The swapped variables in the initial and boundary forcings include SST and METEO (geopotential height, potential temperature, winds, and water vapor mixing ratio). Swapping the selected variables in the two datasets can help identify the role of factors in affecting the morphology of cloud street in a realistic scenario, which usually cannot be achieved by arbitrarily decreasing or increasing the values, although the latter is widely used by many studies to construct sensitivity studies (e.g., an idealized study on entrained aerosols; Chen et al. 2020). One of the challenges associated with this method is to disentangle more than one aspect from one spatial pattern (e.g., SST domain-mean values, gradient). Although it is a challenge to explain all the differences in the morphology of clouds, our analysis shown in section 3 is still helpful to identify impacts of factors on the cloud street morphology.

Sections 3a and 3b show the model–observation comparisons and cloud morphology characterization based on the control simulation (i.e., “ERA5” in Table 1). Section 3c shows the sensitivities of cloud morphology to the forcing datasets. Section 4 summarizes the conclusion and provides the discussions.

3. Results

In this section, we evaluate the WRF simulations of PFCs characteristics and quantify the sensitivity of cloud streets to large-scale forcings. The definition of a few terms and variables used in our analysis are summarized in Table 2.

a. Evaluating WRF simulation with observations

Snapshots of the simulated liquid and all-ice water path are shown in Fig. 3 with the top row showing the outer domain and the bottom row showing the inner domain. There is a large area of clouds covering the eastern part of the outer domain, whereas broken low-cloud deck and cloud streets appear in the inner domain. Those features are consistent with the GOES-16 observations in Fig. 2. From 0801 to 1001 EST, the cloudy area decreases with larger and larger gaps between clouds, demonstrating the dissipation during this period. Similar dissipation also appears in the GOES-16 images. There are small discrepancies in cloud structure between GOES-16

and WRF simulations. The cloudy roll features observed in GOES-16 are visually more curved than those simulated in the model. At 0801 EST, GOES-16 shows cloud streets that extend to the northwest corner of the domain (Fig. 2c), while WRF simulates less cloud coverage for the same area (Fig. 3c). These discrepancies between the model and observations are likely due to unresolved turbulence and convection in the mesoscale model or uncertainties in large-scale forcing datasets (e.g., colder boundary layer in the model in Fig. 5a).

The total water path histogram between the inner domain of the WRF simulation “ERA5” and GOES-16 are comparable (Fig. 4). At 1001 EST, GOES-16 shows a larger probability density between 10 and 100 g m⁻² and a smaller density at larger total water path. The small model overestimation at 1001 EST is likely related to the slightly slower dissipation in the model. We also use dropsonde measurements from the ACTIVATE campaign to evaluate the simulated boundary layer properties (Fig. 5). Both dropsondes and WRF simulations show in the potential temperature (Θ) and water vapor mixing ratio (Q_v) a well-mixed marine boundary layer with the inversion height at ~1.5 km. Despite the relatively colder temperature from the model as compared to measurements at dropsonde locations, moisture and wind are comparable in terms of mean values. The colder temperature might be due to biases in the forcings from ERA5 reanalysis (Seethala et al. 2021). Also, WRF shows smaller spatial variations of Q_v above the boundary layer than dropsondes. Since the WRF simulation reproduces the cloud street structure and generally agree with dropsonde measurements regarding boundary layer properties, we use the simulation “ERA5” as the control simulation to study factors influencing the evolution and mesoscale morphology of cloud streets.

b. Characteristics of postfrontal clouds

The outer domain of our WRF simulations covers a large area, including land, coastal cloud-free areas, PFCs, and the frontal cloud region. The mechanisms and processes of the clear-sky or cloudy conditions are different in different subregions. To better characterize the variations in different cloud spatial structures, we divided the outer domain into six zones based on the

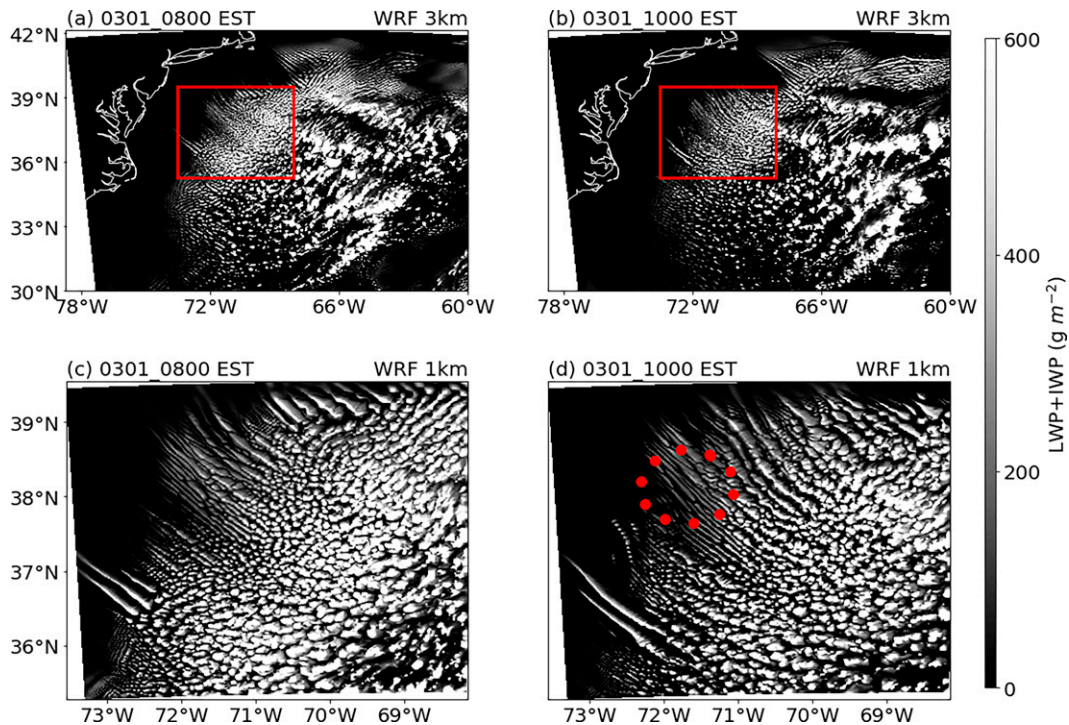


FIG. 3. Liquid and all-ice water path from WRF for (a),(b) the outer domain with a horizontal grid spacing as 3 km and (c),(d) the inner domain with horizontal grid spacing as 1 km at (a),(c) 0801, and (b),(d) 1001 EST. Red dots represent dropsonde locations.

underlying surface (i.e., land-sea type) and cloud patterns at 1000 EST (Fig. 6). The cloud water path is smoothed by a uniform filter of 30 grids, which removes the high-frequency variations in the complex cloud structure. Then we separate out the clear coastal and zones 3–6 with the values of smoothed water path (WP_{sm}) of <40 , 40–200, 200–500, and >500 $g\ m^{-2}$, respectively. Figure 6 demonstrates that this method marks the boundary and

transition of cloud street zones, which also shows a good alignment with the coastal line and the cloud patches in close proximity of the frontal system. The key feature of the cloud pattern in each zone is as the name indicates. The PFC region (i.e., zones 4 and 5) has both the cloud street and other forms of broken shallow cloud coexisting. In zone 4, cloud streets are the primary form, while in zone 5, both cloud streets and open-cell clouds exist.

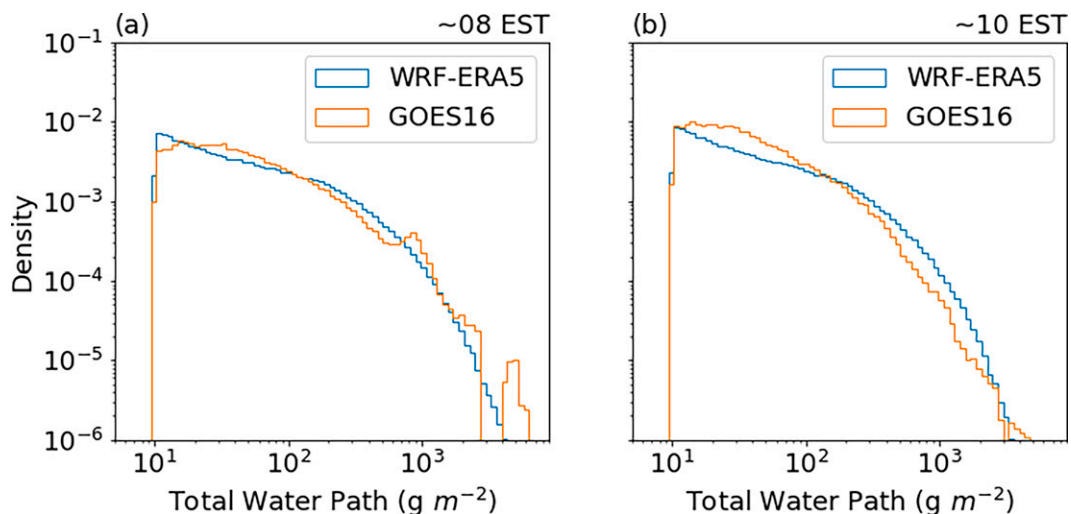


FIG. 4. Probability density function of the total water path at (a) \sim 0800 and (b) \sim 1000 EST from WRF inner domain and *GOES-16* with the same regions as the inner domain of WRF simulation “ERA5.”

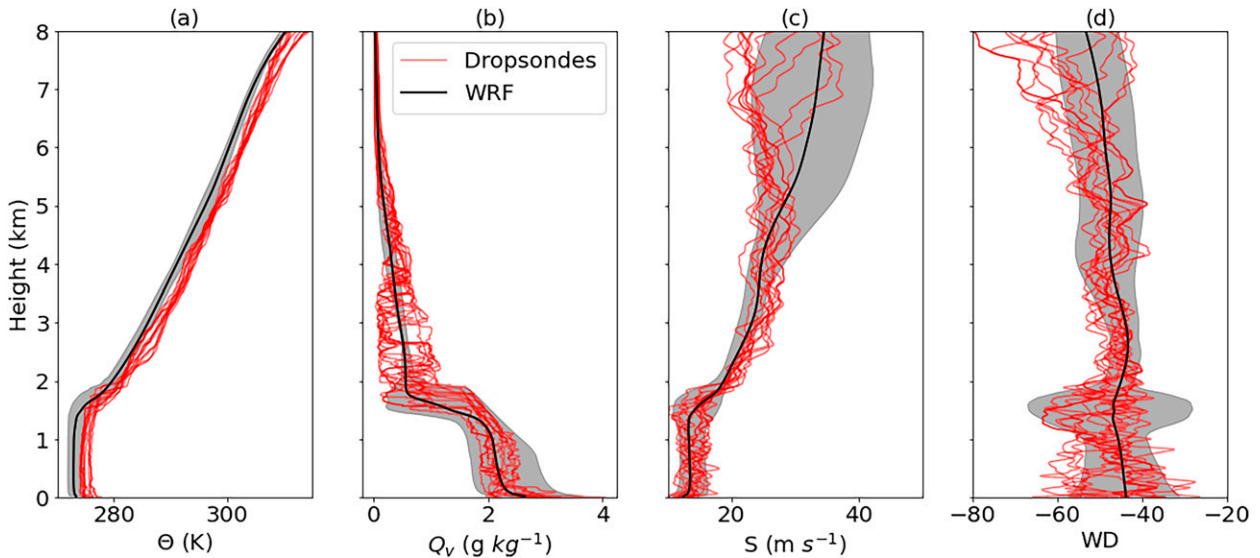


FIG. 5. Profiles of (a) potential temperature Θ , (b) water vapor mixing ratio Q_v , (c) horizontal wind speed S , and (d) horizontal wind direction WD . Black lines are the spatially and temporally (between 0945 and 1045 EST) averaged values from WRF simulation in the smallest box covering dropsonde locations. Gray shading denotes the range of values within the smallest box covering dropsonde locations averaged between 0945 and 1045 EST from the model.

Figure 7 shows the profiles of temperature, moisture, clouds, and dynamical features below 600 hPa at 1000 EST. The inversion cap is found in all zones at ~ 800 – 900 hPa except for the region close to the frontal system. Differences in surface temperature reflect different boundary layer structure at various distances to the frontal system. Generally, the oceanic region (zone 2–6) is featured with more moisture and large horizontal wind speed than the land region (zone 1). The marine boundary layer does not exhibit evident wind speed shear but it shows a strong wind direction shear in all the zones. From land to the frontal system, wind directional shear, comparing winds at the surface to the free troposphere, changes from clockwise to counterclockwise with the transition occurring between the clear sky and the cloud streets, which suggests that a lack of cloud streets into clear sky near the coastal area is likely associated with the direction of wind

direction shear, although the weaker near-surface winds and surface fluxes in zone 2 might play an important role in determining the lack of clouds. Previous studies found that Ekman spiral from horizontal winds leads to horizontal vorticity and favors the formation of roll clouds (e.g., LeMone 1973). The linkage between boundary layer wind shear and cloud street morphology is further explained by the results of sensitivity studies in section 3c. Large-scale ascending motion (i.e., positive vertical wind speed, w) in the frontal cloud region might have led to the compensating subsidence in the postfrontal regions with the zone 5 having the strongest subsidence at ~ 800 hPa (Fig. 7e). The variance of vertical velocity is the largest in the frontal region and becomes larger when getting closer to the frontal system at the PFC region. Except for the frontal system, other regions do not have significant liquid precipitation (dash lines in Fig. 7g) but snow is

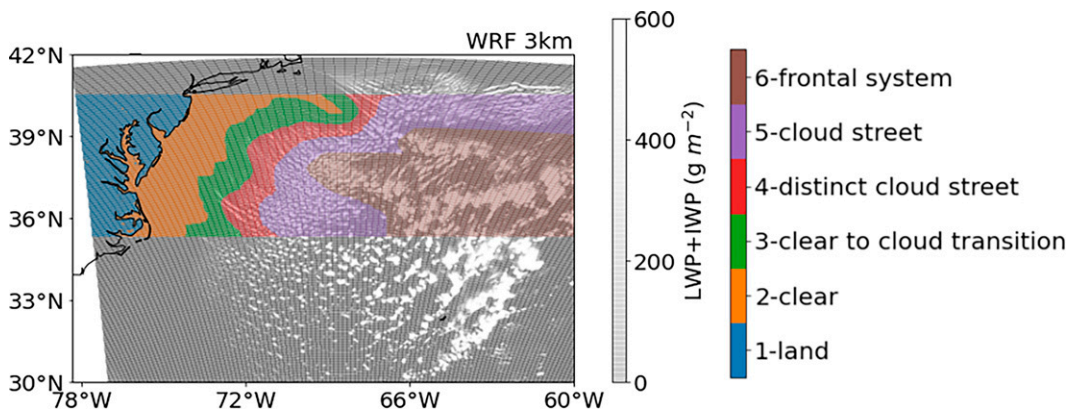


FIG. 6. Various zones with the WRF outer domain defined by the surface and cloud patterns at 1000 EST.

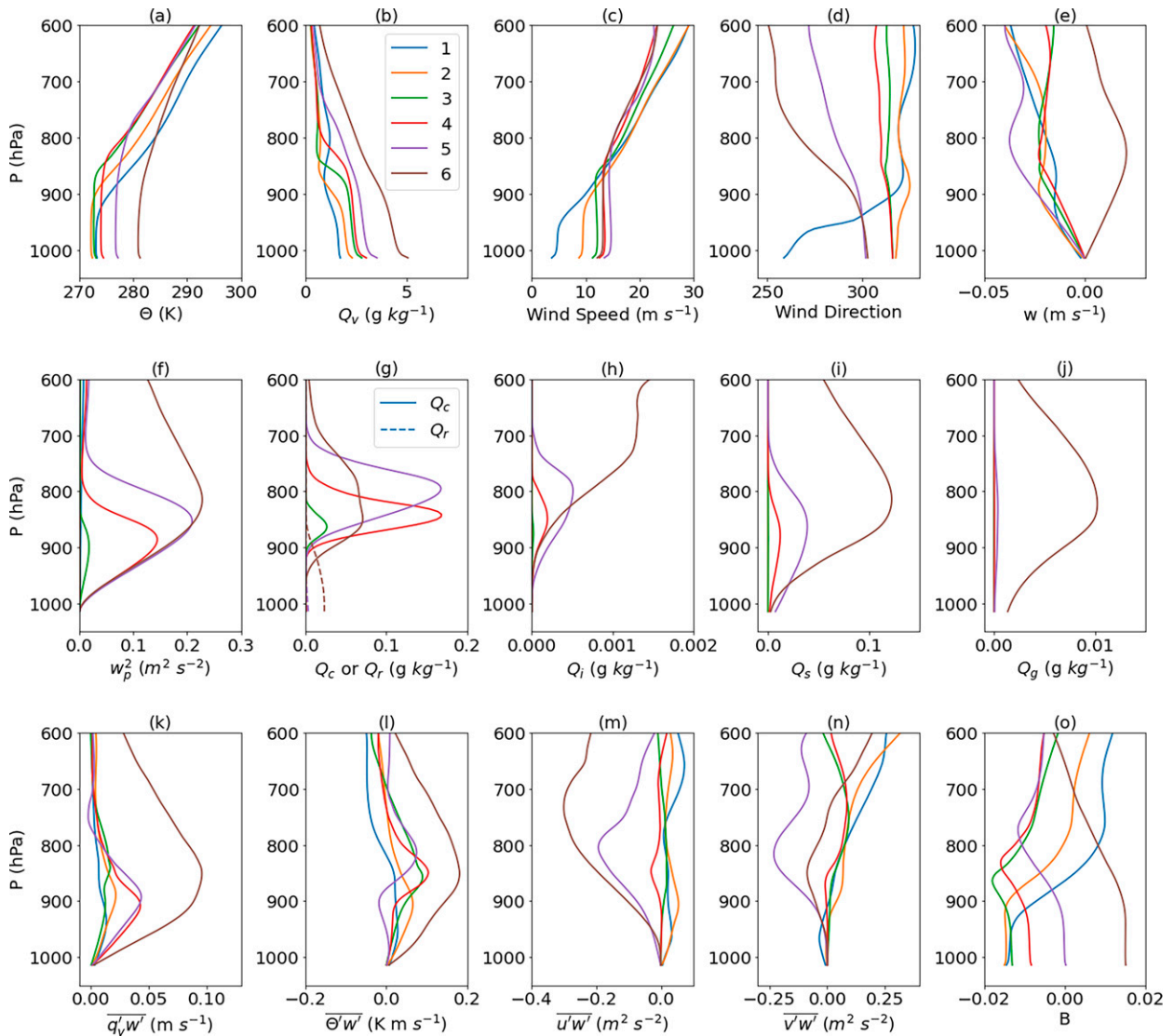


FIG. 7. Comparison of mean profiles of (a) potential temperature, (b) water vapor mixing ratio, (c) horizontal wind speed, (d) horizontal wind direction, (e) vertical velocity, (f) variance of vertical velocity, (g) cloud and rainwater mixing ratio, (h) ice water mixing ratio, (i) snow mixing ratio, (j) graupel mixing ratio, (k) water vapor flux, (l) energy flux, (m) west–east wind flux, (n) northwest wind flux, and (o) buoyancy from the six zones in Fig. 6.

evident in the PFC region. The height of maximum momentum, energy, and moisture transport from zone 1–6 increases generally. All those features indicate multiple factors affecting the formation of the roll structure including, but not limited to, buoyancy and wind direction shear. It is expected that simulating the morphology of roll clouds is related to the representations of SST and meteorological factors in the lateral and surface boundary meteorological conditions.

We quantitatively characterize the morphology of cloud streets in Fig. 8. The probability density function (PDF) of cloud area size distribution, shown in Fig. 8a, suggests a decreasing trend of cloud size with time in the morning and early afternoon. Here we define the cloud mask by the cloud core fraction $WP/WP_{sm} > 0.8$ to quantify the broken level of the cloud deck

without the interference of cloud thickness, where the subscript “sm” denotes “smoothed” cloud field (Table 2). Note that the results do not depend on the choice of the threshold values (i.e., 0.8). The decreasing inversion height with time in Fig. 8a indicates the effect of subsidence in the postfrontal area. Figure 8b shows that the domain-mean total water path from both liquid and all-ice phase has a peak at about 0600 EST but the domain-mean cloud core fraction decreases from 0500 to 1500 EST. During the cloud dissipation, the cloud deck initially breaks. Then the area of clear gaps expands.

The strength of cloud street can be quantified by the shape of the cloud mask quantified by the ratio of the longest dimension to the shortest dimension (i.e., aspect ratio L_1/L_s , Table 2). Figure 8c shows the histograms of L_1/L_s at five

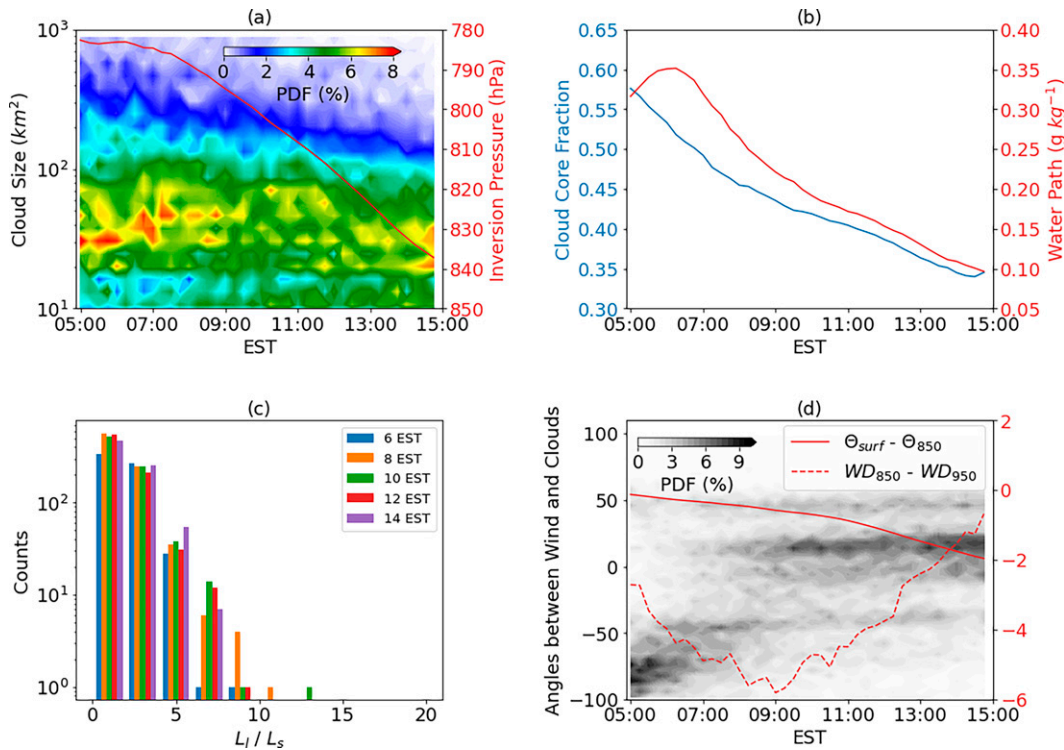


FIG. 8. (a) Time evolution of the PDF of cloud size distribution (shading) and PBL height in pressure coordinate (red line) in the entire inner domain. (b) Time series of the sum of liquid and all-ice water path (i.e., WP) (blue) and cloud core fraction defined by $WP/WP_{sm} > 0.8$ (red). (c) The aspect ratio of the horizontal cloud mask at five snapshots. (d) The angle between cloud alignment and wind direction at 800 hPa (shading, positive means clouds tilt counterclockwise from wind direction, only included $L_1/L_s > 2$), instability (red solid line, domain-mean $\Theta_{surf} - \Theta_{850 \text{ hPa}}$), and wind direction shear (unit: $^\circ$; red dash line, $WD_{850\text{hPa}} - WD_{950\text{hPa}}$ averaged below clouds with $L_1/L_s > 2$).

snapshots. Most clouds have their L_1/L_s between 1 and 2. The percentages of clouds with $L_1/L_s > 2$ are 30.21%, 20.51%, 21.30%, 16.76%, and 21.10% at 0600, 0800, 1000, 1200, 1400 EST, respectively, and the percentages of the long clouds with $L_1/L_s > 6$ are 0.24%, 0.85%, 1.18%, 0.99%, respectively. The most elongated clouds at 1000 EST have L_1/L_s of 12.67. Thus, the dissipation of the clouds between 0500 and 1500 EST can be divided into two stages. The roll clouds are stabilized with the L_1/L_s becoming larger during the first stage, while the roll clouds break and form segments of small cloud patches in the second stage. The dividing time is ~ 1000 EST.

Red lines in Fig. 8d show the instability (solid line) and the wind direction shear (dashed line). The boundary layer becomes more stable during the day. The wind direction shear increases until 0900 EST, suggesting that the dynamical instability from the Ekman spiral plays dominant roles in the formation of the roll clouds in this case. Figure 8d also shows the angles that clouds (only included $L_1/L_s > 4$) tilted clockwise from the wind direction at 800 hPa. Before 0600 EST, most clouds have an angle of $\sim -70^\circ$ (i.e., counterclockwise) to the wind direction. Starting from ~ 0600 EST, clouds have angles around $\sim 14^\circ$ with the majority having the shift after 0900 EST. The dominant angle (i.e., $\sim 14^\circ$) is consistent with theory with dynamical Ekman spiral and assumed neutral stratification (e.g., Atkinson and Zhang 1996).

c. Sensitivities of cloud streets to the large-scale forcings

We have the following hypothesized factors that influence PFC cloud amount and morphology: 1) the thermal factor: heating from surface turbulent fluxes in the morning triggers or strengthens convection and mixing in the marine boundary layer; and 2) the meteorological factor: wind and moisture content over the PFC region play a role in affecting the cloud morphology and, especially, wind direction shear causes the formation of the Ekman spiral and horizontal vorticities. To examine the role of these two factors, we analyze the sensitivities of cloud evolution and morphology to the surface fluxes and large-scale meteorological fields. To design the sensitivity experiments in a more realistic manner, we use different analysis/reanalysis forcing datasets, including ERA5 and FNL, to drive the model simulations, instead of imposing an arbitrary perturbation.

The spatial distributions of SST between FNL and ERA5 are different (an example at 0100 EST in Fig. 9). In the inner domain, where cloud streets and open-cellular clouds coexist in a few hours during the simulation time, ERA5 has a larger SST in the center (along the Gulf Stream) and a lower SST to the north and south, leading to a stronger SST gradient and larger spatial variability. Here we use three more simulations in addition to the control simulation (i.e., “ERA5”) as

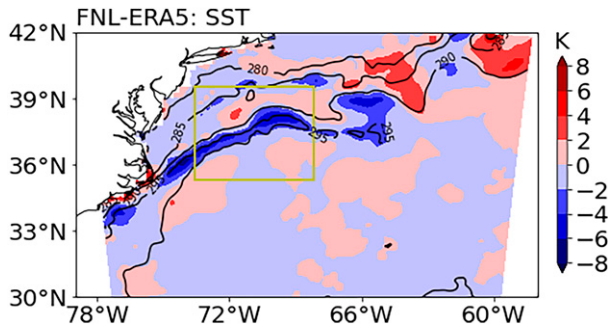


FIG. 9. Spatial distribution of the differences of initial sea surface temperature (SST) between FNL and ERA5. The black contours represent SST from ERA5. The box marks the inner model domain.

summarized in Table 1: 1) driven by ERA5 except for FNL SST, i.e., “ERA5(FNL_SST)”;

2) driven by FNL, i.e., “FNL”;

and 3) driven by FNL except for ERA5 SST, i.e., “FNL(ERA5_SST).” Switching SST from ERA5 to FNL leads to smaller total water path, while switching SST from FNL to ERA5 leads to larger total water path (Fig. 10a). The subscript “swap” in Fig. 10 means swapping the corresponding variables with another forcing datasets.

Besides SST, meteorological factors are also expected to impact the cloud street morphology, including wind, Θ , and Q_v . Figure 11 shows the differences in the wind speed, wind direction, Θ , and Q_v from ERA5 and FNL, respectively. ERA5 shows larger wind speed with more westerly wind in the boundary layer. Figures 11c and 11f show that ERA5 provides higher values of wind speed up to ~ 800 – 850 hPa and stronger wind direction shear in the layer between 950 and 800 hPa. In the inner domain, ERA5 and FNL show small differences at 1000 hPa but FNL shows a lower value of the Θ at 850 hPa (Figs. 11g,h). The profiles from Fig. 11i show that FNL provides a deeper mixing layer than ERA5. ERA5 shows a drier and warmer PBL than FNL does. Such drier and warmer PBL are consistent with Figs. 11h and 11k. The higher values of wind direction (i.e., more westerly) might come from a different balance state with different temperature and moisture. Simulations with swapped initial and boundary layer wind, pressure, Θ , and Q_v field show that the large-scale meteorological field from FNL has their largest water path earlier than 0500 EST but the total water path after 0600 EST did not change. All the factors that lead to the major different time series of hydrometeor water path (WP) have been included in the SST and METEO sensitivity tests because the results from ERA5(FNL_METEO)

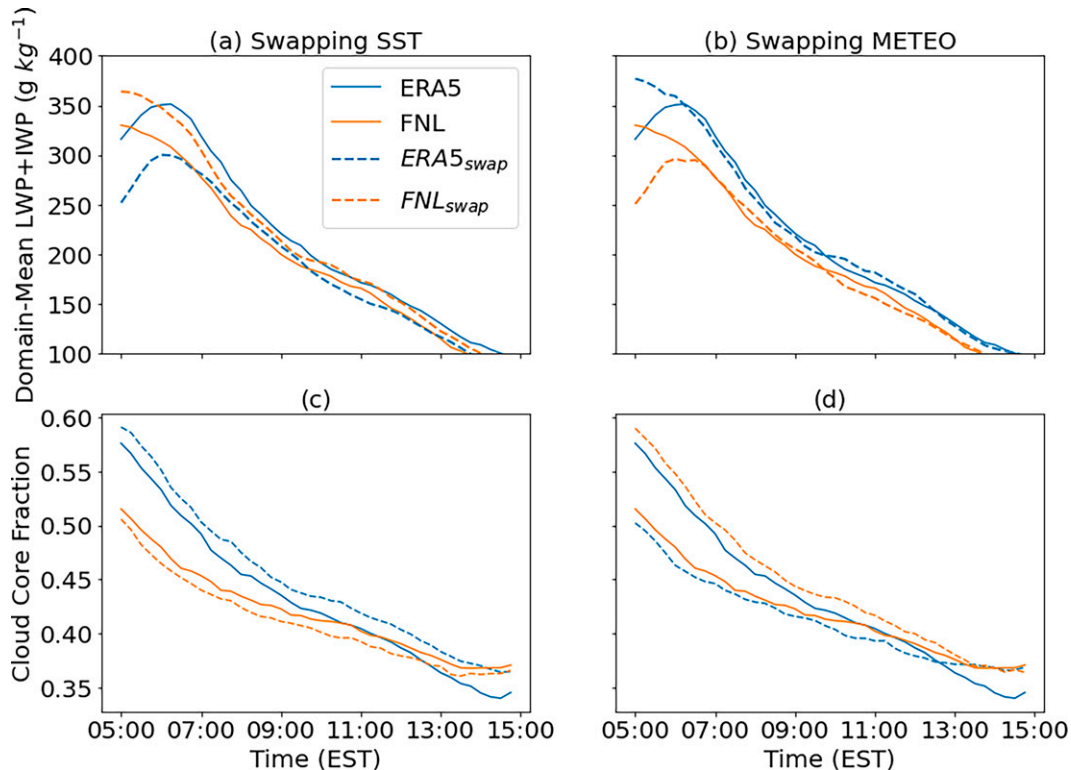


FIG. 10. (a),(b) Time series of total water path (LWP + IWP) from the inner domain of WRF simulations with different forcing datasets. The blue solid line here is the same as the red line in Fig. 8. (c),(d) Time series of the fraction of model grids with the ratio of $WP/WP_{sm} > 0.8$ from the inner domain of WRF simulations with different forcing datasets. The subscript “swap” means swapping the corresponding variables with another forcing datasets, for example, dashed blue lines in (a) and (b) refer to simulation “ERA5(FNL_SST)” and “ERA5(FNL_METEO)” in Table 1, respectively.

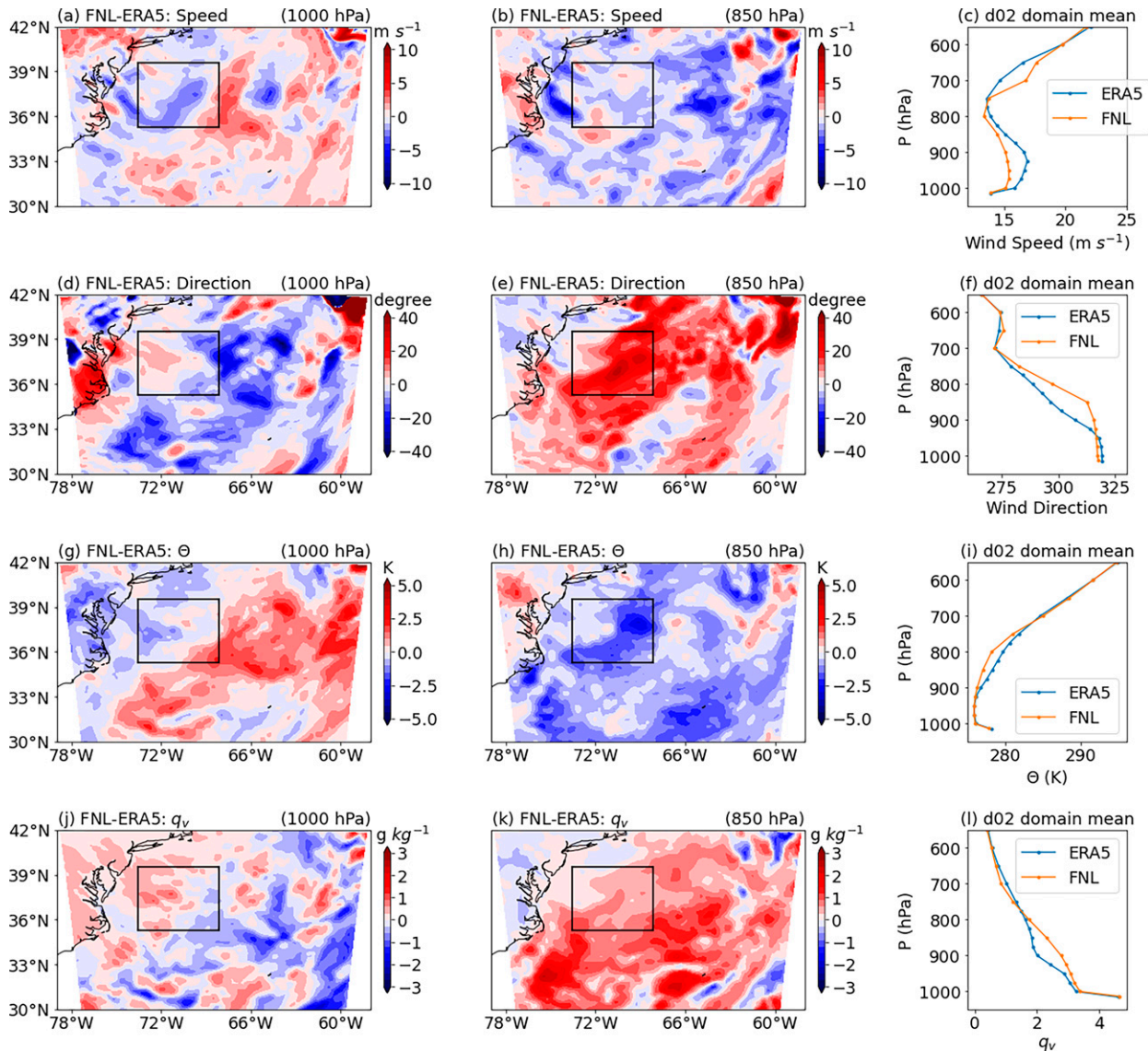


FIG. 11. (left),(center) Spatial distribution of the differences of initial (a),(b) wind speed, (d),(e) wind direction, (g),(h) potential temperature, and (j),(k) water vapor mixing ratio between ERA5 and FNL at (a),(d),(g),(j) 1000 and (b),(e),(h),(k) 850 hPa. (right) Profiles of the inner domain (i.e., d02) mean (c) wind speed, (f) wind direction, (i) potential temperature, and (l) water vapor mixing ratio.

is similar to FNL(ERA_SST) (Figs. 10a,b). Those two simulations are identical except for the land surface conditions and other numerical differences (i.e., the vertical grid spacing).

The cloud core fraction from the sensitivity studies are shown in Figs. 10c and 10d. Swapping SST from FNL to ERA5 leads to smaller domain-mean total water path but larger cloud core fraction (Figs. 10a,c). Smaller total water path indicates thinner clouds and larger cloud core fraction indicates larger horizontal extend of clouds. Figure 12 confirms that the SST pattern from FNL leads to a larger size of cloud mask between 0700 and 0900 EST. During the early afternoon, swapping SST does not show big differences in clouds (Fig. 12) because clouds become thinner overall at this time and the selection of thresholds for calculating the cloud mask

becomes more challenging, which suggests the cloud core fraction in Figs. 10c and 10d is a better measure of the cloud broken level. Another pair of simulations with the FNL forcings and with ERA5 SST plus the remaining FNL forcings (orange lines), respectively, show consistent results with the simulations based on ERA5. Meteorology (METEO) from FNL leads to lower core fraction before 1300 EST indicating smaller cloud size (Fig. 12).

FNL has a smaller value of domain-mean SST (i.e., 0.32 K differences for outer domain and 0.86 K differences for inner domain) and weaker SST gradient than ERA5, which leads to smaller domain-mean water path but larger cloud core fraction. The former is likely due to the weaker boundary layer instability and shallower boundary layer (i.e., higher inversion

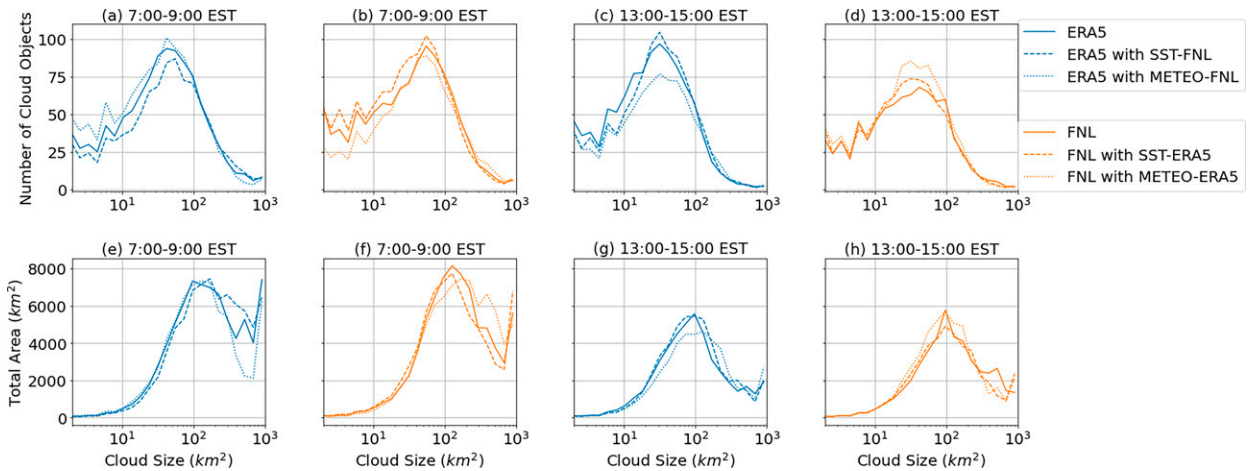


FIG. 12. Size distribution of (a)–(d) number of cloud objects and (e)–(h) cloud area in the (a),(b),(e),(f) early morning and (c),(d),(g),(h) early afternoon.

pressure due to the lower domain-mean SST, as shown in Fig. 13). The latter is likely due to the mechanism reported in previous studies that the smaller latent heat flux gradients lead to weaker cloud-top entrainment, which slows down the dissipation and leads to larger cloud core fraction (Zheng et al. 2021; Sandu and Stevens 2011; Xiao et al. 2011). Figures 10b and 10d show the impacts of large-scale winds; swapping METEO brings the core fraction close to each other but barely changes the domain-mean water path. Because METEO includes the impacts of both wind and moisture, it is hard to tell why METEO from FNL leads to lower cloud core fraction.

One possible explanation is that FNL has higher inversion level in the early morning but similar values in late morning (Fig. 13c), indicative of a more pronounced inversion height drop during the morning, which is likely the reason for a lower cloud core fraction when using METEO from FNL in Fig. 10d.

Mesoscale circulations associated with cloud streets are analyzed in Fig. 14. The cloudy area is defined by aspect ratio $L_1/L_y > 2$. The clear gaps are within 5 km away from the edge of the cloudy rolls. Convergence is associated with roll clouds, while divergence is associated with the clear region below ~900 hPa. Above ~900 hPa, convergence occurs with the

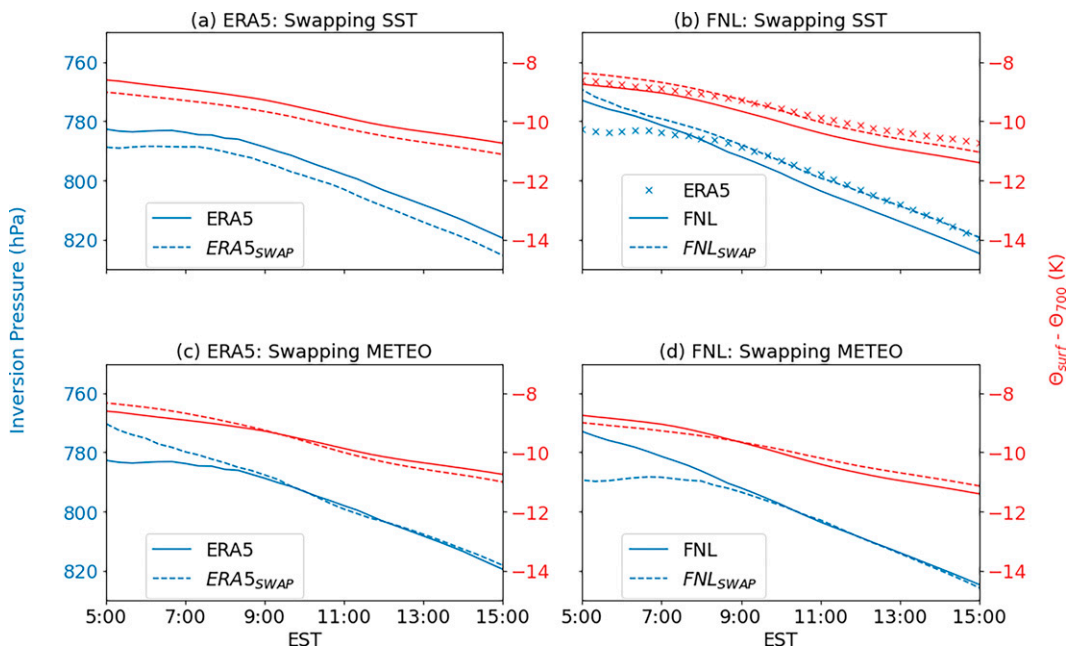


FIG. 13. Time series of LST and inversion height for all the sensitivity simulations. The cross markers in (b) are the same as the solid lines in (a) to show the differences between ERA5 and FNL forcing datasets.

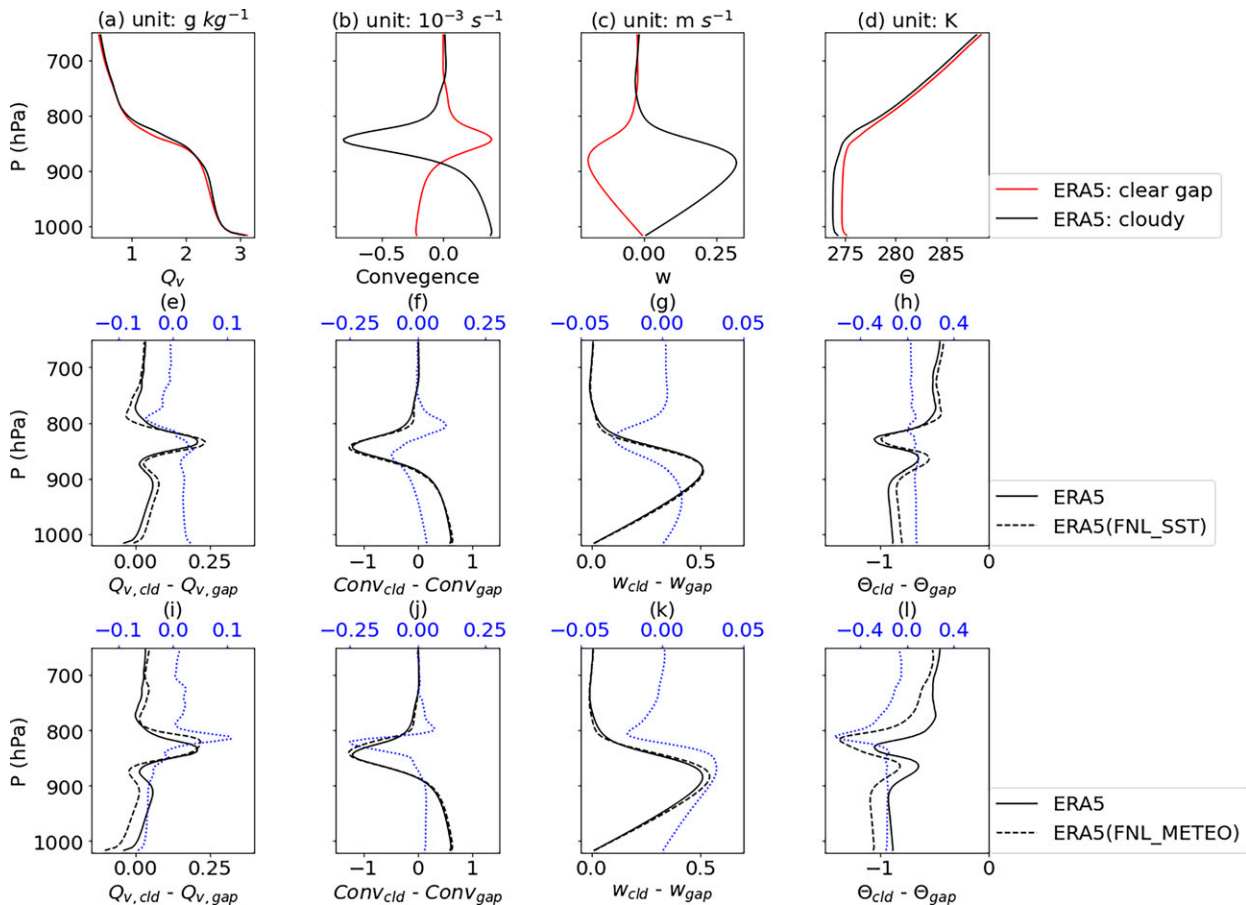


FIG. 14. (a)–(d) Averaged profiles of Q_v , convergence, w , and Θ at cloudy rolls and clear gaps. (e)–(l) Differences of variables between cloudy rolls and clear gaps. Blue lines represent the difference between sensitivity and control simulations.

clear region while divergence occurs with cloudy rolls. Cloudy rolls are associated with upward cold moist air, while clear gaps are associated with downward dry warm air. The differences of variables between cloudy rolls and the clear gaps indicate the strength of mesoscale circulation and their transportation of energy. SST from FNL does not lead to significant impacts on the convergence and w , but causes larger differences of Q_v and smaller differences of Θ . FNL has a smaller domain-mean SST and smaller gradient. The latter leads to smaller differences of Θ . Note that the difference of SST between the region below cloudy rolls and clear gaps is -1.4 K for simulation “ERA5” but -0.9 K for “ERA5(FNL_SST)” as shown in Table 3. A larger difference of Q_v might be caused by the differences of latent heat

flux between the region below cloudy rolls and clear gaps, that is -59.5 $W m^{-2}$ for “ERA5” and -41.4 $W m^{-2}$ for “ERA5(FNL_SST).” METEO from FNL leads to larger differences in w than SST from FNL, indicating a slightly stronger mesoscale circulation. Also, METEO from FNL leads to a drier PBL below clouds than the clear gaps and a larger difference of Θ . The complex differences in the METEO make it challenging to explain the detailed mechanisms behind those differences.

In section 3b, we showed that the strongest roll structure occurs ~ 1 h after the strongest wind direction shear. Figure 15 examines it in the sensitivity simulations. When the METEO from ERA5 is applied, there is a maximum of wind direction shear and a maximum fraction of long rolls at 0945 EST. Long

TABLE 3. Differences of SST, surface sensible heat fluxes (HFX), and latent heat fluxes (LH) in control and sensitivity simulations. Numbers are in the following order: clear gaps, cloudy rolls, and the differences (cloudy roll minus clear gaps).

Simulation	SST (K)	HFX ($W m^{-2}$)	LH ($W m^{-2}$)
ERA5	291.9, 290.5, -1.4	286.6, 279.6, -7.0	535.3, 475.8, -59.5
ERA5(FNL_SST)	290.8, 289.9, -0.9	265.8, 262.7, -3.1	483.4, 442.0, -41.4
ERA5(FNL_METEO)	292.6, 292.1, -0.5	306.1, 305.1, -1.0	583.6, 548.0, -35.6

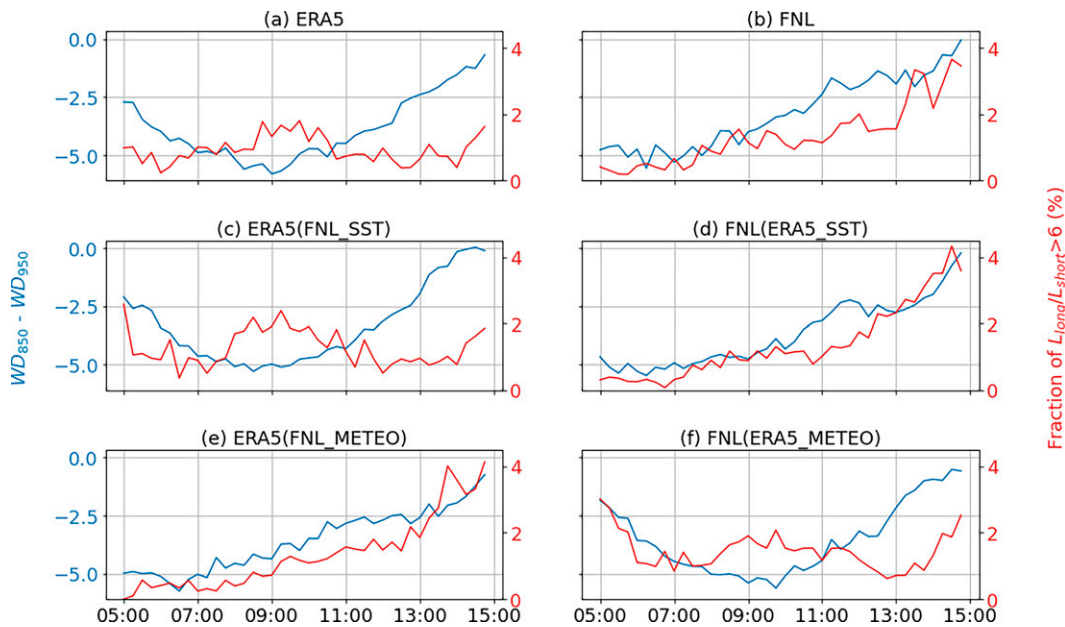


FIG. 15. Time series of the wind direction shear between 850 and 950 hPa (blue curves) and the fraction of $L_1/L_s > 6$ (red curves) for all simulations. Wind direction shear is calculated in the same way as the red dashed line in Fig. 8d.

rolls are defined here as $L_1/L_s > 6$. When the METEO from FNL is applied, wind direction shear decreases, and the fraction of long rolls increases almost monotonically. Figure 16 shows the differences in the angle between cloud alignment and wind direction between the sensitivity simulations and the control simulations. In both “ERA5” and “FNL,” clouds are mainly concentrated at an angle of 50° to the right of wind angle in the early morning. After about 0900 EST, when the cloud street starts to form, clouds align on the angle of 14° to the left of the mean wind angle. The impacts of the SST pattern on the distribution of this angle are not as evident as those from METEO. The METEO from FNL leads to fewer clouds at 14° to the left of wind direction in the early afternoon (Figs. 16c,f), which is consistent with weak wind direction shear in the early afternoon. Figures 15 and 16 indicate that the wind direction shear peak can only be simulated with the METEO from ERA5, which is critical to better simulate the cloud streets in this PFC event.

4. Conclusions

In this study, we examine the morphology of postfrontal clouds in the western North Atlantic Ocean (WNAO) on 1 March 2020 during the Aerosol Cloud Meteorology Interactions over the Western Atlantic Experiment (ACTIVATE). We use the Weather Research and Forecasting (WRF) Model to investigate how the differences in initial and boundary conditions impact the morphology of cloud streets during the PFC event. We found that the differences of both SST and meteorological factors between two large-scale datasets drive different cloud amounts and cloud street morphology during the dissipation of PFC clouds. Those sensitivities of postfrontal low clouds to the large-scale driving forcings provide new

insights into improving the representations of such clouds in future simulations, such as the importance of SST gradient and wind direction shear.

We compare the total liquid and ice water path between *GOES-16* and WRF Model with ERA5 as the large-scale forcings to evaluate the model simulations. The cloud pattern from the model is consistent with *GOES-16* in that cloud streets prevail in the same region as our inner domain and open-cell clouds are to the downwind of the cloud streets. The histogram of total water path is also consistent between *GOES-16* and WRF (with ERA5 forcing). We also compare dropsonde measurements during ACTIVATE with WRF simulated meteorological profiles. We found that they are consistent with each other except that the simulated potential temperature is slightly colder in the boundary layer, which might relate to a small cold bias in ERA5. Overall ERA5 captures the large-scale features well and provides accurate initial and boundary forcings to the WRF mesoscale model compared to *GOES-16* and dropsonde measurements.

Cloud street morphology is quantitatively investigated from various aspects. During the dissipation stage of postfrontal cloud streets, total water path and cloud core fraction decrease along with cloud size. The cloud streets prevail between 0800 and 1200 EST. The ratio of the longest dimension to the shortest dimension (i.e., the aspect ratio of cloud horizontal mask) ranges from 1 to 12.67. The angle between cloud streets and the mean winds at 800 hPa is $\sim 14^\circ$ during the prevailing stage. Wind direction shear is the strongest at about 0900 EST when the $\sim 14^\circ$ starts to form, which suggests that Ekman spiral effect in the boundary layer contributes to the formation of the cloud streets in this PFC case.

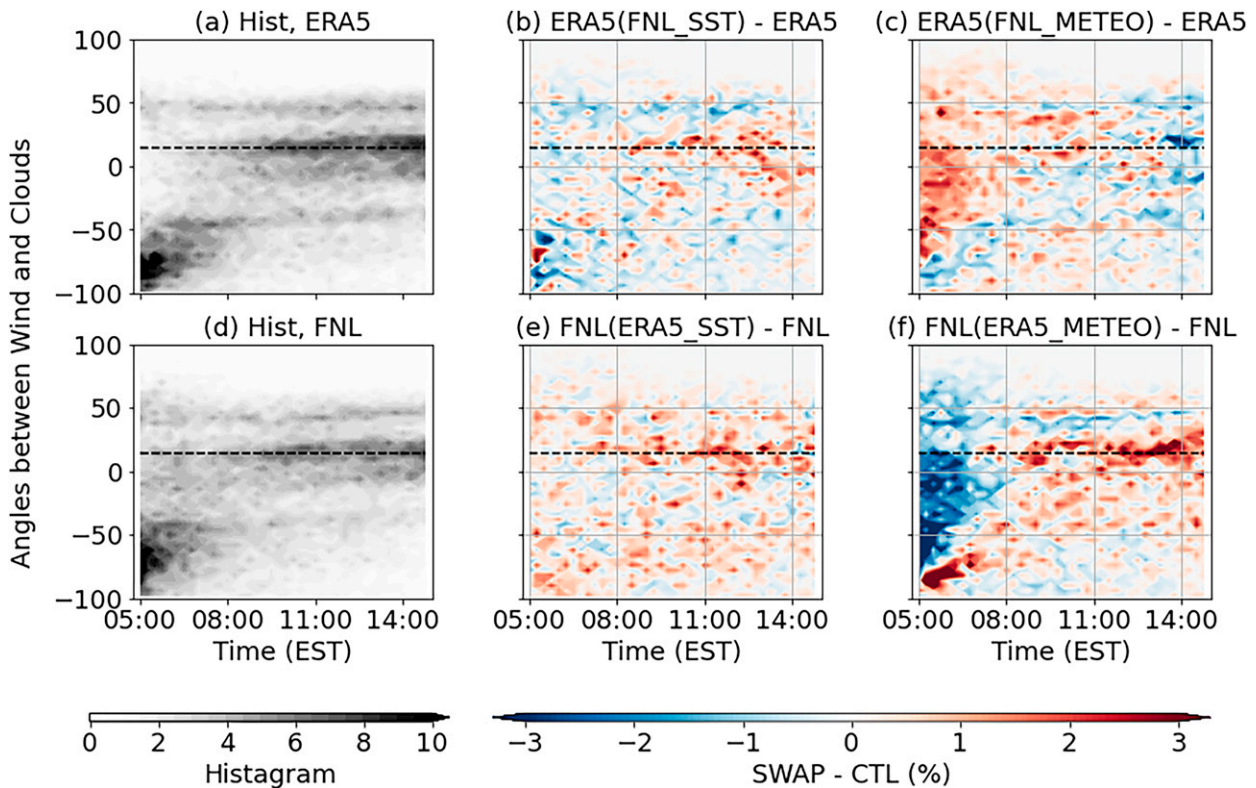


FIG. 16. Differences of the angle between cloud alignment and wind direction in sensitivity simulations and the control simulations. The way to calculate the angle between cloud alignment and wind direction is the same as the shading in Fig. 8d. The dashed black lines mark the angle at 14° .

We construct the sensitivity simulations by swapping SST and meteorological factors between ERA5 reanalysis data and FNL analysis data. ERA5 has a warmer SST and larger spatial gradient between the gulf stream and its surrounding regions than FNL. The SST from ERA5 leads to a higher hydrometeor water path and lower cloud core fraction. The former is explained by stronger instability induced by larger SST gradient and/or larger SST domain mean, and the latter might relate to a larger gradient of latent heat flux that induces the entrainment of dry air. The meteorological factors, including wind, temperature, and water vapor, are different in many aspects, for example, the wind direction shear. We found that the ERA5 data lead to a peak wind direction shear, which contributes to a maximum in the fraction of long rolls and contributes to more cloud streets staying at $\sim 14^\circ$ with 800 hPa mean wind.

This study shows that large-scale forcings impact the simulated morphology of cloud streets through SST and meteorological factors such as wind shear. SST modifies the instability of the boundary layer and contributes to cloud formation. Wind shear affects more on the persistence of roll structure through the Ekman spiral. Besides those factors we have discussed in this study, cloud-top entrainment is also usually thought to be critical in determining the transition from stratiform clouds to the broken cumulus clouds (Zheng et al. 2021), which warrants further investigation.

Acknowledgments. This work was supported through the ACTIVATE Earth Venture Suborbital-3 (EVS-3) investigation, which is funded by NASA's Earth Science Division and managed through the Earth System Science Pathfinder Program Office. The Pacific Northwest National Laboratory (PNNL) is operated for the U.S. Department of Energy by Battelle Memorial Institute under Contract DE-AC05-76RLO1830. The simulations were performed using resources available through Research Computing at PNNL.

Data availability statement. ACTIVATE data are publicly available from NASA website (<https://www-air.larc.nasa.gov/cgi-bin/ArcView/activate.2019>). The WRF community model was made available from the National Center for Atmospheric Research (NCAR) at <http://www2.mmm.ucar.edu/wrf/users/>. WRF Model output (4 Tb) in this study is saved on PNNL's long-term storage system, Aurora (rc-support@pnnl.gov). A subset of analyzed data are also available from Zenodo (<https://doi.org/10.5281/zenodo.5907514>).

REFERENCES

- Abel, S. J., and Coauthors, 2017: The role of precipitation in controlling the transition from stratocumulus to cumulus clouds in a Northern Hemisphere cold-air outbreak. *J. Atmos. Sci.*, **74**, 2293–2314, <https://doi.org/10.1175/JAS-D-16-0362.s1>.

- Agee, E. M., 1987: Mesoscale cellular convection over the oceans. *Dyn. Atmos. Oceans*, **10**, 317–341, [https://doi.org/10.1016/0377-0265\(87\)90023-6](https://doi.org/10.1016/0377-0265(87)90023-6).
- Atkinson, B. W., and J. W. Zhang, 1996: Mesoscale shallow convection in the atmosphere. *Rev. Geophys.*, **34**, 403–431, <https://doi.org/10.1029/96RG02623>.
- Babić, N., and S. F. De Wekker, 2019: Characteristics of roll and cellular convection in a deep and wide semiarid valley: A large-eddy simulation study. *Atmos. Res.*, **223**, 74–87, <https://doi.org/10.1016/j.atmosres.2019.03.009>.
- Bandhauer, M., and Coauthors, 2021: Evaluation of daily precipitation analyses in E-OBS (v19.0e) and ERA5 by comparison to regional high-resolution datasets in European regions. *Int. J. Climatol.*, **42**, 727–747, <https://doi.org/10.1002/joc.7269>.
- Chen, F., and J. Dudhia, 2001: Coupling an advanced land surface–hydrology model with the Penn State–NCAR MM5 modeling system. Part I: Model implementation and sensitivity. *Mon. Wea. Rev.*, **129**, 569–585, [https://doi.org/10.1175/1520-0493\(2001\)129<0569:CAALSH>2.0.CO;2](https://doi.org/10.1175/1520-0493(2001)129<0569:CAALSH>2.0.CO;2).
- Chen, J., Y. Liu, and M. Zhang, 2020: Effects of lateral entrainment mixing with entrained aerosols on cloud microphysics. *Geophys. Res. Lett.*, **47**, e2020GL087667, <https://doi.org/10.1029/2020GL087667>.
- Chen, Y., H. Yuan, and S. Gao, 2019: A high-resolution simulation of roll convection over the Yellow Sea during a cold air outbreak. *J. Geophys. Res. Atmos.*, **124**, 10 608–10 625, <https://doi.org/10.1029/2019JD030968>.
- Chlond, A., 1992: Three-dimensional simulation of cloud street development during a cold air outbreak. *Bound.-Layer Meteor.*, **58**, 161–200, <https://doi.org/10.1007/BF00120757>.
- Chou, S.-H., and M. P. Ferguson, 1991: Heat fluxes and roll circulations over the western Gulf Stream during an intense cold-air outbreak. *Bound.-Layer Meteor.*, **55**, 255–281, <https://doi.org/10.1007/BF00122580>.
- Dadashazar, H., and Coauthors, 2021: Cloud drop number concentrations over the western North Atlantic Ocean: Seasonal cycle, aerosol interrelationships, and other influential factors. *Atmos. Chem. Phys.*, **21**, 10 499–10 526, <https://doi.org/10.5194/acp-21-10499-2021>.
- Endo, S., and Coauthors, 2015: RACORO continental boundary layer cloud investigations: 2. Large-eddy simulations of cumulus clouds and evaluation with in situ and ground-based observations. *J. Geophys. Res. Atmos.*, **120**, 5993–6014, <https://doi.org/10.1002/2014JD022525>.
- Etling, D., and R. A. Brown, 1993: Roll vortices in the planetary boundary layer: A review. *Bound.-Layer Meteor.*, **65**, 215–248, <https://doi.org/10.1007/BF00705527>.
- Fast, J. D., and Coauthors, 2019: Overview of the HI-SCALE field campaign: A new perspective on shallow convective clouds. *Bull. Amer. Meteor. Soc.*, **100**, 821–840, <https://doi.org/10.1175/BAMS-D-18-0030.1>.
- Field, P. R., R. J. Cotton, K. Mcbeath, A. P. Lock, S. Webster, and R. P. Allan, 2014: Improving a convection-permitting model simulation of a cold air outbreak. *Quart. J. Roy. Meteor. Soc.*, **140**, 124–138, <https://doi.org/10.1002/qj.2116>.
- , and Coauthors, 2017: Exploring the convective grey zone with regional simulations of a cold air outbreak. *Quart. J. Roy. Meteor. Soc.*, **143**, 2537–2555, <https://doi.org/10.1002/qj.3105>.
- Foken, T., 2006: 50 years of the Monin–Obukhov similarity theory. *Bound.-Layer Meteor.*, **119**, 431–447, <https://doi.org/10.1007/s10546-006-9048-6>.
- Gryschka, M., and S. Raasch, 2005: Roll convection during a cold air outbreak: A large eddy simulation with stationary model domain. *Geophys. Res. Lett.*, **32**, L14805, <https://doi.org/10.1029/2005GL022872>.
- , J. Fricke, and S. Raasch, 2014: On the impact of forced roll convection on vertical turbulent transport in cold air outbreaks. *J. Geophys. Res. Atmos.*, **119**, 12 513–12 532, <https://doi.org/10.1002/2014JD022160>.
- Harris, L. M., and D. R. Durran, 2010: An idealized comparison of one-way and two-way grid nesting. *Mon. Wea. Rev.*, **138**, 2174–2187, <https://doi.org/10.1175/2010MWR3080.1>.
- Hersbach, H., and Coauthors, 2020: The ERA5 global reanalysis. *Quart. J. Roy. Meteor. Soc.*, **146**, 1999–2049, <https://doi.org/10.1002/qj.3803>.
- Hong, S.-Y., and J.-O. J. Lim, 2006: The WRF single-moment 6-class microphysics scheme (WSM6). *J. Korean Meteor. Soc.*, **42**, 129–151.
- Iacono, M. J., J. S. Delamere, E. J. Mlawer, M. W. Shephard, S. A. Clough, and W. D. Collins, 2008: Radiative forcing by long-lived greenhouse gases: Calculations with the AER radiative transfer models. *J. Geophys. Res.*, **113**, D13103, <https://doi.org/10.1029/2008JD009944>.
- Kawase, H., T. Sato, and F. Kimura, 2005: Numerical experiments on cloud streets in the lee of island arcs during cold-air outbreaks. *Geophys. Res. Lett.*, **32**, L14823, <https://doi.org/10.1029/2005GL023256>.
- Kazemirad, M., and M. A. Miller, 2020: Summertime post-cold-frontal marine stratocumulus transition processes over the eastern North Atlantic. *J. Atmos. Sci.*, **77**, 2011–2037, <https://doi.org/10.1175/JAS-D-19-0167.1>.
- Lai, H. W., F. Zhang, E. E. Clothiaux, D. R. Stauffer, B. J. Gaudet, J. Verlinde, and D. Chen, 2020: Modeling Arctic boundary layer cloud streets at grey-zone resolutions. *Adv. Atmos. Sci.*, **37**, 42–56, <https://doi.org/10.1007/s00376-019-9105-y>.
- Lamraoui, F., J. F. Booth, C. M. Naud, M. P. Jensen, and K. L. Johnson, 2019: The interaction between boundary layer and convection schemes in a WRF simulation of post cold frontal clouds over the ARM east North Atlantic site. *J. Geophys. Res. Atmos.*, **124**, 4699–4721, <https://doi.org/10.1029/2018JD029370>.
- LeMone, M. A., 1973: The structure and dynamics of horizontal roll vortices in the planetary boundary layer. *J. Atmos. Sci.*, **30**, 1077–1091, [https://doi.org/10.1175/1520-0469\(1973\)030<1077:TSADOH>2.0.CO;2](https://doi.org/10.1175/1520-0469(1973)030<1077:TSADOH>2.0.CO;2).
- Li, X.-Y., and Coauthors, 2021: Large-eddy simulations of marine boundary-layer clouds associated with cold-air outbreaks during the ACTIVATE campaign. Part I: Case setup and sensitivities to large-scale forcings. *J. Atmos. Sci.*, **79**, 73–100, <https://doi.org/10.1175/JAS-D-21-0123.1>.
- Liu, A. Q., G. W. Moore, K. Tsuboki, and I. A. Renfrew, 2004: A high-resolution simulation of convective roll clouds during a cold-air outbreak. *Geophys. Res. Lett.*, **31**, L03101, <https://doi.org/10.1029/2003GL018530>.
- Mason, P. J., 1983: On the influence of variations in Monin–Obukhov length on horizontal roll vortices in an inversion-capped planetary boundary layer. *Bound.-Layer Meteor.*, **27**, 43–68, <https://doi.org/10.1007/BF00119971>.
- Mechem, D. B., Y. L. Kogan, and D. M. Schultz, 2010: Large-eddy simulation of post-cold-frontal continental stratocumulus. *J. Atmos. Sci.*, **67**, 3835–3853, <https://doi.org/10.1175/2010JAS3467.1>.

- Minnis, P., and Coauthors, 2008: Near-real time cloud retrievals from operational and research meteorological satellites. *Proc. SPIE*, **7107**, 710703, <https://doi.org/10.1117/12.800344>.
- , and Coauthors, 2011: CERES edition-2 cloud property retrievals using TRMM VIRS and Terra and Aqua MODIS data—Part I: Algorithms. *IEEE Trans. Geosci. Remote Sens.*, **49**, 4374–4400, <https://doi.org/10.1109/TGRS.2011.2144601>.
- , and Coauthors, 2021: CERES MODIS cloud product retrievals for edition 4—Part I: Algorithm changes. *IEEE Trans. Geosci. Remote Sens.*, **59**, 2744–2780, <https://doi.org/10.1109/TGRS.2020.3008866>.
- Morrison, I., S. Businger, P. Dodge, and J. A. Businger, 2005: An observational case for the prevalence of roll vortices in the hurricane boundary layer. *J. Atmos. Sci.*, **62**, 2662–2673, <https://doi.org/10.1175/JAS3508.1>.
- National Centers for Environmental Prediction, 2000: NCEP FNL operational model global tropospheric analyses, continuing from July 1999. NCAR RDA, accessed 1 March 2022, <https://doi.org/10.5065/D6M043C6>.
- Naud, C. M., J. F. Booth, and A. D. Del Genio, 2014: Evaluation of ERA-Interim and MERRA cloudiness in the Southern Ocean. *J. Climate*, **27**, 2109–2124, <https://doi.org/10.1175/JCLI-D-13-00432.1>.
- , —, and F. Lamraoui, 2018: Post cold frontal clouds at the ARM eastern North Atlantic site: An examination of the relationship between large-scale environment and low-level cloud properties. *J. Geophys. Res. Atmos.*, **123**, 12 117–12 132, <https://doi.org/10.1029/2018JD029015>.
- Painemal, D., and Coauthors, 2021a: An overview of atmospheric features over the western North Atlantic Ocean and North American east coast—Part 2: Circulation, boundary layer, and clouds. *J. Geophys. Res. Atmos.*, **126**, e2020JD033423, <https://doi.org/10.1029/2020JD033423>.
- , and Coauthors, 2021b: Evaluation of satellite retrievals of liquid clouds from the GOES-13 imager and MODIS over the midlatitude North Atlantic during the NAAMES campaign. *Atmos. Meas. Tech.*, **14**, 6633–6646, <https://doi.org/10.5194/amt-14-6633-2021>.
- Salesky, S. T., M. Chamecki, and E. Bou-Zeid, 2017: On the nature of the transition between roll and cellular organization in the convective boundary layer. *Bound.-Layer Meteor.*, **163**, 41–68, <https://doi.org/10.1007/s10546-016-0220-3>.
- Sandu, I., and B. Stevens, 2011: On the factors modulating the stratocumulus to cumulus transitions. *J. Atmos. Sci.*, **68**, 1865–1881, <https://doi.org/10.1175/2011JAS3614.1>.
- Seethala, C., and Coauthors, 2021: On assessing ERA5 and MERRA2 representations of cold-air outbreaks across the Gulf Stream. *Geophys. Res. Lett.*, **48**, e2021GL094364, <https://doi.org/10.1029/2021GL094364>.
- Skamarock, W. C., and Coauthors, 2019: A description of the Advanced Research WRF Model version 4. NCAR Tech. Note NCAR/TN-556+STR, 145 pp., <https://doi.org/10.5065/1dfh-6p97>.
- Sorooshian, A., and Coauthors, 2019: Aerosol–cloud–meteorology interaction airborne field investigations: Using lessons learned from the U.S. West Coast in the design of activate off the U.S. East Coast. *Bull. Amer. Meteor. Soc.*, **100**, 1511–1528, <https://doi.org/10.1175/BAMS-D-18-0100.1>.
- , and Coauthors, 2020: Atmospheric research over the western North Atlantic Ocean region and North American East Coast: A review of past work and challenges ahead. *J. Geophys. Res. Atmos.*, **125**, e2019JD031626, <https://doi.org/10.1029/2019JD031626>.
- Spensberger, C., and T. Spengler, 2021: Sensitivity of air-sea heat exchange in cold-air out-breaks to model resolution and sea-ice distribution. *J. Geophys. Res. Atmos.*, **126**, e2020JD033610, <https://doi.org/10.1029/2020JD033610>.
- Tarek, M., F. P. Brissette, and R. Arsenault, 2020: Evaluation of the ERA5 reanalysis as a potential reference dataset for hydrological modelling over North America. *Hydrol. Earth Syst. Sci.*, **24**, 2527–2544, <https://doi.org/10.5194/hess-24-2527-2020>.
- Walter, B. A., and J. E. Overland, 1984: Observations of longitudinal rolls in a near neutral atmosphere. *Mon. Wea. Rev.*, **112**, 200–208, [https://doi.org/10.1175/1520-0493\(1984\)112<0200:OOLRIA>2.0.CO;2](https://doi.org/10.1175/1520-0493(1984)112<0200:OOLRIA>2.0.CO;2).
- Wang, H., and G. Feingold, 2009: Modeling mesoscale cellular structures and drizzle in marine stratocumulus. Part I: Impact of drizzle on the formation and evolution of open cells. *J. Atmos. Sci.*, **66**, 3237–3256, <https://doi.org/10.1175/2009JAS3022.1>.
- Williams, K. D., and Coauthors, 2013: The transpose-AMIP II experiment and its application to the understanding of Southern Ocean cloud biases in climate models. *J. Climate*, **26**, 3258–3274, <https://doi.org/10.1175/JCLI-D-12-00429.1>.
- Wu, C., and J. Chen, 2021: Simulation of aerosol indirect effects on cloud streets over the north-western Pacific Ocean. *J. Geophys. Res. Atmos.*, **126**, e2020JD034325, <https://doi.org/10.1029/2020JD034325>.
- Xiao, H., C. M. Wu, and C. R. Mechoso, 2011: Buoyancy reversal, decoupling and the transition from stratocumulus to shallow cumulus topped marine boundary layers. *Climate Dyn.*, **37**, 971–984, <https://doi.org/10.1007/s00382-010-0882-3>.
- Zheng, Y., H. Zhang, and Z. Li, 2021: Role of surface latent heat flux in shallow cloud transitions: A mechanism-denial study. *J. Atmos. Sci.*, **78**, 2709–2723, <https://doi.org/10.1175/JAS-D-20-0381.1>.
- Zurn-Birkhimer, S. M., E. M. Agee, and Z. Sorbjan, 2005: Convective structures in a cold air outbreak over Lake Michigan during Lake-ICE. *J. Atmos. Sci.*, **62**, 2414–2432, <https://doi.org/10.1175/JAS3494.1>.